Smart Structures and Systems, *Vol. 34*, *No. 6* (*2024*) *367-376*
https://doi.org/10.12989/sss.2024.34.6.367

Frequencies and modal shapes analysis of multi-point supported beam structures for a resonator sensitive component

Wenhua Hu [1,2,3], Yibao Cai [2,3], Ruiqin Wu*[2,3], Jianen Chen [2,3], Jingjing Feng [2,3] and Guofeng Xia**[1]

[1] *Chongqing Three Gorges University*, *Chongqing 404120*, *P.R. China*
[2] *Tianjin Key Laboratory for Advanced Mechatronic System Design and Intelligent Control*, *School of Mechanical Engineering*, *Tianjin University of Technology*, *Tianjin 300384*, *P.R. China*
[3] *National Demonstration Center for Experimental Mechanical and Electrical Engineering Education*, *Tianjin University of Technology*, *Tianjin 300384*, *P.R. China*

(*Received July 7*, *2024*, *Revised December 22*, *2024*, *Accepted December 28*, *2024*)

Abstract. Multi-supported beam structures are widely used in engineering applications, particularly as sensitive components in resonators. The intrinsic properties of these sensitive components significantly influence the performance of resonators. In this study, a dynamic theoretical model of a multi-point supported beam was established, considering the impact of the supported beams on the overall structure. The governing equations of motion of the multi-point supported beam structure were derived using the Hamiltonian principle. A theoretical method was proposed to calculate frequencies and global modal shapes of the multi-point supported beam structures. The theoretical results were validated through numerical simulations with specific parameters. The natural frequencies of a multi-point supported beam were also experimentally measured and compared with the simulation results. Our investigation into the effects of structural parameters on the frequency and global modal shapes demonstrated the effectiveness of the proposed method. The findings show that frequencies and modal shapes of the complex beam undergo regular changes as structural parameters vary. This study provides a theoretical foundation for improving the performance of beam resonators and serves as a guide for the parametric design of multi-point supported beam structures.

Keywords: experiment; frequency; global modal shape; multi-point supported beam; resonator sensitive component

1. Introduction

Microelectromechanical systems (MEMS) integrate mechanical components with microelectronics and find widespread applications in fields such as medical devices, automobiles, and industrial control systems (Hossain *et al.* 2024). Hajjaj *et al.* (2020) emphasized that understanding the linear and nonlinear dynamical behaviors of movable structures in MEMS is crucial for their successful implementation. Resonators serve as the crucial working elements within MEMS, and the mechanical models of their sensitive components are often simplified into microscale beams, plates, or rings (Ranji *et al.* 2023). Based on those models, the frequencies and modal shapes of the sensitive components in the resonator can be theoretically analyzed, which is beneficial to their structural design and control.

Beams are commonly employed as sensitive components in resonators. A model of resonators consisting of beams has been developed to detect the nonlinear dynamics (Alattar *et al.* 2023), and an energy harvester with zigzag beams has been proposed to lower resonant frequency and broaden bandwidth (Feng *et al.* 2023). Usually, these sensitive components in resonators are fixed by supported structures, which can lead to energy dissipation (Romero *et al.* 2020). Analytical model of support loss in a rocking mass resonator has been developed and verified (Wang *et al.* 2011). Energy transmission from the vibrating resonator to the support in micromechanical resonators has been determined using two-dimensional elastic wave theory (Chen *et al.* 2017). Recent studies have explored the effects of axial pre-tension and nonlinear vibration properties on support loss in doubly clamped beam resonators (Ma *et al.* 2024). Considering the influence of the supported structures, the sensitive components of beam resonators should be dynamically modelled as multi-point supported complex beam structures.

Complex beam structures are widely used in engineering, including atomic force microscopes (Raman *et al.* 2008), resonators (Vyas *et al.* 2009) and energy harvester (Erturk *et al.* 2009). Previous theoretical studies have addressed simple configurations, such as L-shaped beams with the in-plane model (Cao *et al.* 2015) and the out-of-plane model (Georgiades *et al.* 2013). Karami and Inman (2011) proposed a zigzag harvester and calculated its modal shapes. Iliuk *et al.* (2014) analyzed the modal energy transferring in a portal frame structure. Dou and Jensen (2016) presented a method to tune the hardening/softening behavior of three-beam structures, while Danzi *et al.* (2018) examined the orientation of members in multi-beam resonators. Kumar *et al.* (2024) simplified several folding supported beams of a bandpass filter into a spring and stated

---

*Corresponding author, Ph.D., Associate Professor, E-mail: ruiqinwu@163.com

**Co-corresponding author, Ph.D., Associate Professor, E-mail: xiaguofeng@sanxiau.edu.cn

http://www.techno-press.org/?journal=sss&subpage=7

ISSN: 1738-1584 (Print), 1738-1991 (Online)

that nonlinear modal coupling via internal resonances in resonators has been widely used to improve performance. These studies generally focus on cascade architectures; however, as dynamical models of beam resonators, multi-point supported complex beams often involve parallel structures.

Frequencies and modal shapes are critical characteristics of resonators that can significantly impact their performance (Thrust 2025). For instance, the dynamic behavior of graphene micro ribbons shows that natural frequencies decrease with increased mass intensity in a fixed position (Mohammadimehr and Monajemi 2016). Nonlinear viscoelastic damping effects on cantilever sensors and system frequency responses have also been investigated (Habib *et al*. 2022). Mode localization in two coupled resonators was studied through experimental and theoretical analyses (Liu *et al*. 2024). The equations have been derived governing the dynamic behavior of MEMS devices, with a focus on the analysis of natural frequencies (Akhavan *et al*. 2022). While analytical modal shapes for straight beams are relatively straightforward to calculate, multi-beam structures pose additional complexity (Zhang *et al*. 2016). Studies have focused on analytical modal shapes for L-shaped beams (Warminski *et al*. 2008), relative error measurements (Tripathi and Bajaj 2013), and comparisons with ANSYS (Zhou *et al*. 2017). Jujjuvarapu *et al*. (2024) analyzed a resonator with a regular hexagon-shaped beam and a cantilever beam. However, there is limited research on the theoretical analysis of frequencies and modal shapes for multi-point supported beam structures.

The influences of the supported structure on the frequencies and global modal shapes of a beam resonator are considered, and the beam resonator has been modeled using a multi-point supported beam structure with parallel configuration. The governing equations of motion and boundary conditions of the system are obtained, and the frequencies and global modal shapes of the structure are analyzed. Additionally, the frequencies of a multi-point supported beam structure are experimentally measured. The parametric laws of the frequencies and modal shapes for the structure are explored, which may provide a theoretical basis for optimizing the parameters of multi-point supported beam structures, such as beam resonators.

2. Theoretical model

The sensitive component of a resonator is modeled as a multi-point supported beam and the position vectors are described. Subsequently, the governing equations and corresponding boundary conditions of the beam are obtained with the Hamilton principle. Fig. 1(a) shows the sensitive component of a multi-point supported beam resonator, which consists of a resonant beam and three supported beams. The exciting electrodes are arranged on the lower side of the resonant beam to mainly excite its bending vibration, and their positions are dependent on the vibration mode of the resonant beam. The resonant beam may work in the second-order bending vibration mode. One end of the supported beam is connected to the node of the vibration mode of the resonant beam, and the other end is a fixed anchor point. As shown in Fig. 1(b), the global coordinate system is defined at the anchor point of the left supported beam so that the axes of each part are in the same plane before the deformation. The multi-point supported beam can be divided into seven parts, and the local coordinate system of each part is defined as $o_ix_iy_iz_i$. The length, width and height of the ith part are L_i, b_i and h_i.

In order to investigate the vibration characteristics of the structure, the following assumptions are proposed:

(1) Each part of the structure is considered as an isotropic homogeneous equal-section Euler-Bernoulli beam,

(2) The effect of gravity is not considered.

The variables u_i, v_i, w_i respectively represent displacements along axes of x_i, y_i, z_i, and θ_i is the rotation around the x_i axis. The position vectors of a point at the axis of each part are described as

$$\begin{cases} \boldsymbol{R}_1 = [x_1 + u_1 \quad v_1 \quad w_1]^T \\ \boldsymbol{R}_2 = \boldsymbol{R}_1(L_1) + \boldsymbol{T}_2[x_2 + u_2 \quad v_2 \quad w_2]^T \\ \boldsymbol{R}_3 = \boldsymbol{R}_2(L_2) + \boldsymbol{T}_3[x_3 + u_3 \quad v_3 \quad w_3]^T \\ \boldsymbol{R}_4 = \boldsymbol{R}_2(L_2) + \boldsymbol{T}_4[x_4 + u_4 \quad v_4 \quad w_4]^T \\ \boldsymbol{R}_5 = \boldsymbol{R}_1(L_1) + \boldsymbol{T}_5[x_5 + u_5 \quad v_5 \quad w_5]^T \\ \boldsymbol{R}_6 = \boldsymbol{R}_5(L_5) + \boldsymbol{T}_6[x_6 + u_6 \quad v_6 \quad w_6]^T \\ \boldsymbol{R}_7 = \boldsymbol{R}_5(L_5) + \boldsymbol{T}_7[x_7 + u_7 \quad v_7 \quad w_7]^T \end{cases} \tag{1}$$

where, L_i is the length of ith part. $\mathbf{T}_i$ is used to transform displacements in the ith local coordinate into the global coordinate, whose linear parts are:

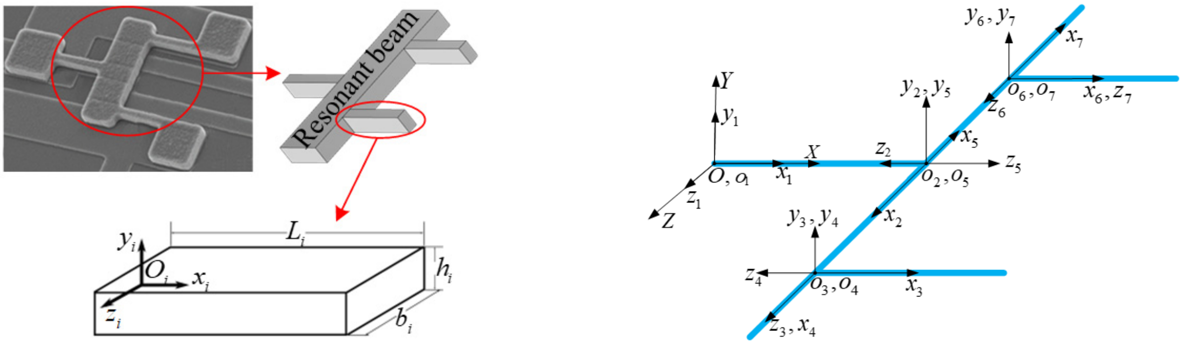

(a) The sensitive structure (b) A multi-point supported beam

Fig. 1 A resonator with multiple anchors

$$\boldsymbol{T}_2=\begin{bmatrix}-w_1'(L_1) & -v_1'(L_1) & -1\\ -\theta_1 & 1 & -v_2'(L_1)\\ 1 & \theta_1 & -w_1'(L_1)\end{bmatrix} \tag{2a}$$

$$\boldsymbol{T}_3=\begin{bmatrix}1 & -v_1'-\theta_2 & -w_1'-w_2'\\ v_1'+\theta_2 & 1 & v_2'-\theta_1\\ w_1'+w_2' & -v_2'+\theta_1 & 1\end{bmatrix}\Bigg\|_{x_1=L_1}^{x_2=L_2} \tag{2b}$$

$$\boldsymbol{T}_4=\begin{bmatrix}-w_1'-w_2' & -v_1'-\theta_2 & -1\\ v_2'-\theta_1 & 1 & -v_1'-\theta_2\\ 1 & -v_2'+\theta_1 & -w_1'-w_2'\end{bmatrix}\Bigg\|_{x_1=L_1}^{x_2=L_2} \tag{2c}$$

$$\boldsymbol{T}_5=\begin{bmatrix}w_1' & -v_1' & 1\\ \theta_1 & 1 & v_1'\\ -1 & \theta_1 & w_1'\end{bmatrix}\Bigg\|_{x_1=L_1} \tag{2d}$$

$$\boldsymbol{T}_6=\begin{bmatrix}1 & -v_1'+\theta_5 & -w_1'-w_5'\\ v_1'-\theta_5 & 1 & -v_5'-\theta_1\\ w_1'+w_5' & v_5'+\theta_1 & 1\end{bmatrix}\Bigg\|_{x_1=L_1}^{x_5=L_5} \tag{2e}$$

$$\boldsymbol{T}_7=\begin{bmatrix}w_1'+w_5' & -v_1'+\theta_5 & 1\\ v_5'+\theta_1 & 1 & v_1'-\theta_5\\ -1 & v_5'+\theta_1 & w_1'+w_5'\end{bmatrix}\Bigg\|_{x_1=L_1}^{x_5=L_5} \tag{2f}$$

Considering the free vibration of the structure, the kinetic energy and elastic potential energy are calculated, and substituting them into Hamilton's equation, there are

$$\int_{t_1}^{t_2}\delta I\,dt=\int_{t_2}^{t_2}\delta\left(\sum_{i=1}^{7}\int_0^{L_i}H_i dx_i\right)dt=\int_{t_2}^{t_2}\delta\left\{\sum_{i=1}^{7}\int_0^{L_i}\frac{1}{2}\left[\rho_i\left|\dot{\boldsymbol{R}}_i\right|^2-E_iA_iu_i'^2+\sum_{\chi=\xi,\eta,\zeta}\left(\rho_iJ_{i\chi}\omega^2{}_{i\chi}-K_{i\chi}\kappa^2{}_{i\chi}\right)\right]dx_i\right\}dt=0 \tag{3}$$

where, H_i is a function introduced to simplify the calculation. The prime and dot denote spatial and temporal derivatives, respectively. ρ_i is the density. $J_{i\xi}$, $J_{i\eta}$ and $J_{i\zeta}$ stand for the principal mass moments of inertia. $\omega_{i\xi}$, $\omega_{i\eta}$ and $\omega_{i\zeta}$, indicate the angular velocities. $K_{i\xi}$, is the torsional rigidity. $K_{i\eta}$ and $K_{i\zeta}$ are the bending rigidities. $\kappa_{i\xi}$, $\kappa_{i\eta}$ and $\kappa_{i\zeta}$ denote the curvatures. E_i represents the elastic modulus. A_i is the cross-section area. The specific expressions are given in Appendix A.

By substituting Eqs. (1)-(2) into Eq. (3), the equations of motion of the multi-point supported beam and the corresponding boundary conditions can be derived. The boundary conditions are shown in Appendix B. The equations of motion are as follows

$$\begin{cases}\dfrac{\partial^2 H_i}{\partial\dot{u}_i\partial t}+\dfrac{\partial^2 H_i}{\partial u_i'\partial x_i}=0\\[2ex] \dfrac{\partial^3 H_i}{\partial\dot{w}_i'\partial x_i\partial t}+\dfrac{\partial^3 H_i}{\partial w_i'\partial {x_i}^2}-\dfrac{\partial^2 H_i}{\partial\dot{w}_i\partial t}-\dfrac{\partial^2 H_i}{\partial w_i'\partial x_i}=0\\[2ex] \dfrac{\partial^2 H_i}{\partial\dot{\theta}_i\partial t}+\dfrac{\partial^2 H_i}{\partial\theta_i'\partial x_i}=0\\[2ex] \dfrac{\partial^3 H_i}{\partial\dot{v}_i'\partial x_i\partial t}+\dfrac{\partial^3 H_i}{\partial v_i''\partial {x_i}^2}-\dfrac{\partial^2 H_i}{\partial\dot{v}_i\partial t}-\dfrac{\partial^2 H_i}{\partial v_i'\partial x_i}=0\end{cases} \tag{4}$$

In Eq. (4), u_i and θ_i are governed by second-order differential equations and two boundary conditions, whereas, v_i and w_i are governed by fourth-order differential equations and have four boundary conditions. Therefore, there are 28 variables to describe the free vibration of the multi-point supported beam.

3. Modal shapes and frequencies

The governing equations of motion of the beam are linearized to theoretically calculate the modal shapes and frequencies, which are validated by comparing with numerical results.

3.1 Calculation of frequencies and modal shapes

To study the intrinsic properties of the structure, neglecting the nonlinear term in Eq. (4), there are

$$\begin{cases}\ddot{u}_i^*-\dfrac{E_i}{\rho_i}u_i^{*''}=0\\[2ex] \ddot{w}_i^*+\dfrac{E_iJ_{i\eta}}{\rho_iA_i}w_i^{*(4)}-\dfrac{J_{i\eta}}{A_i}\ddot{w}_i^{*''}=0\\[2ex] \ddot{\theta}_i^*-\dfrac{K_{i\xi}}{J_{i\xi}}\theta_i^{*''}=0\\[2ex] \ddot{v}_i^*+\dfrac{E_iJ_{i\zeta}}{\rho_iA_i}v_i^{*(4)}-\dfrac{J_{i\zeta}}{A_i}\ddot{v}_i^{*''}=0\end{cases} \tag{5}$$

where the variables with a star are given in Appendix C.

Based on Eq. (5), it is found that the free vibration of a multi-point supported beam can be decoupled into in-plane and out-of-plane motion. u_i and w_i are coupled in the $o_ix_iz_i$ plane, whereas θ_i and v_i are coupled in the $o_ix_iy_i$ plane.

The variables in Eq. (5) are separated as

$$\begin{cases}{u_i}^*=U_i(x_i){q_i}^u(t), & {w_i}^*=W_i(x_i){q_i}^w(t)\\ {v_i}^*=V_i(x_i){q_i}^v(t), & {\theta_i}^*=\Theta_i(x_i){q_i}^\theta(t)\end{cases} \tag{6}$$

The linear coupling leads to a synchronized motion of the whole structure. Therefore, there are

$$\frac{\ddot{q_i}^u}{{q_i}^u}=\frac{\ddot{q_i}^w}{{q_i}^w}=-{\omega_w}^2,\quad \frac{\ddot{q_i}^v}{{q_i}^v}=\frac{\ddot{q_i}^\theta}{{q_i}^\theta}=-{\omega_v}^2 \tag{7}$$

Substituting Eqs. (6)-(7) into Eq. (5), we have the global modal shapes as follows

$$\begin{cases}U_i(x_i)=\displaystyle\sum_{j=1}^{2}C_{ij}^u e^{\lambda_{ij}^u x_i}, & W_i(x_i)=\displaystyle\sum_{j=1}^{4}C_{ij}^w e^{\lambda_{ij}^w x_i}\\ V_i(x_i)=\displaystyle\sum_{j=1}^{4}C_{ij}^v e^{\lambda_{ij}^v x_i}, & \Theta_i(x_i)=\displaystyle\sum_{j=1}^{2}C_{ij}^\theta e^{\lambda_{ij}^\theta x_i}\end{cases} \tag{8}$$

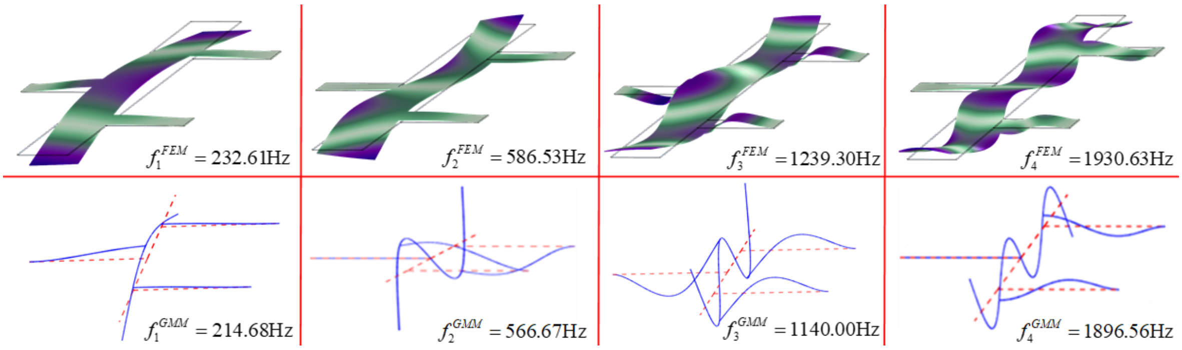

Fig. 2 First four modal shapes of the resonant beam in the *YOZ* plane

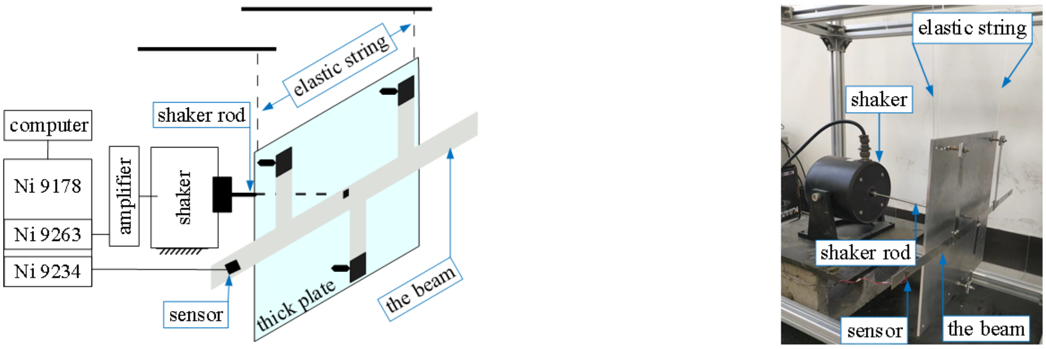

Fig. 3 First four modal shapes of the resonant beam in the *YOZ* plane

where, λ_{ij}^{u}, λ_{ij}^{v}, λ_{ij}^{w} and λ_{ij}^{θ} are given in Appendix D.

By using Eq. (8) and its boundary conditions to compute C_{ij}^{u}, C_{ij}^{v}, C_{ij}^{w} and C_{ij}^{θ}, the frequencies and the global modal shapes of the structure can be obtained analytically.

3.2 Examples and validation

To verify the analytical results, the multi-point supported beam is assumed to have parameters as: ρ_i = 2329 kg/m^3, E_i = 170 GPa, μ_i = 0.28, $L_1 = L_3 = L_6$ = 93 mm, $L_2 = L_4 = L_5 = L_7$ = 50.75 mm, $b_1 = b_3 = b_6$ = 12 mm, $b_2 = b_4 = b_5 = b_7$ = 60 mm, h_i = 1 mm, i = 1...7. The frequencies and global modal shapes of the multi-point supported beam are calculated and compared with the simulations by using the COMSOL software. Because the resonant beam is mainly excited by the electrodes to deform in the *YOZ* plane, the first four orders of bending mode of the resonant beam in the *YOZ* plane are given in Fig. 2. In the simulations, the black lines indicate the undeformed state of the structure, and the displacements from small to large are indicated by the white gradient to blue. In the analytical results, the red dashed lines indicate the undeformed states, and the blue solid lines indicate the global modal shapes. It can be seen that the theoretical and numerical frequencies are close to each other, and the analytical modal shapes are in good agreement with their simulations. The number of nodes in the first four vibration modes of the resonant beam is increased from 2 to 5. The join points of the supported beams are designed at the vibration node of the resonant beam to minimize energy dissipation. The second-order modal shape has three nodes, which is suitable for the resonant beam to have three supported beams at its nodes. For the second-order vibration mode, the midpoint of the resonant beam is a node, where the supported beam has almost no bending deformation. Bending and torsional deformations simultaneously exist if the connections of bilateral supported beams with the resonant beam deviate from the nodes. Obviously, the connection positions of the supported beams may affect the modal shapes, frequency, and nodal distribution of the vibration mode of the structure. The deviation of the connection position of the supported beams from the nodes will lead to more energy dissipation of the resonator, which in turn is unfavorable to the performance of the resonator. In fact, the simulations show that the nodal lines in the resonant beam are not actually along its width direction because there is no symmetric plane in the width direction of the structure.

4. Experimental tests

The first three natural frequencies of a multi-pointed supported beam are tested in the experiments as shown in Fig. 3. The experimental setup includes a computer, a shaker (DH40200), an amplifier (DH5872), the acceleration sensors (PCB352A21/352A73) and NI9178/9234/9263. The multi-pgoint supported beam is made by aluminum strips, which is mounted on a thick aluminum plate with three bolts. The way in which the three ends of the supported beams are fixed on the thick plate is used to approximate the boundary conditions of the theoretical model. For conveniently moving the joints, the supported beams are

Table 1 Parameters of structure Φ_i

	Φ_0	Φ_1	Φ_2	Φ_3
L_2/ mm	150	120	90	60
L_4/ mm	100	100	100	100
L_5/ mm	150	180	210	240
L_7/ mm	100	100	100	100

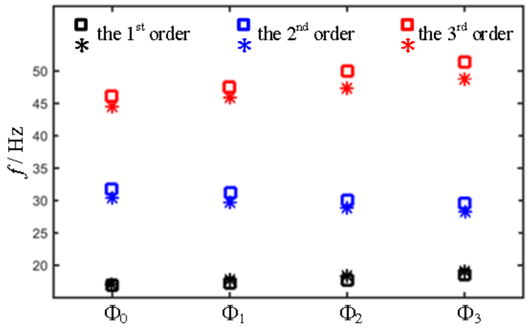

Fig. 4 Comparison of frequencies

designed to use bolts to connect the resonant beam, which is a little different from the structure in Fig. 1. The thick plate is suspended by elastic strings and excited by the shaker in a horizontal direction, which works as a foundation excitation for the multi-point supported beam. Therefore, the beam is excited orthogonally to the gravity, which causes the vibration to decouple from the effect of gravity.

To compare the frequencies obtained from experiments and simulations, the parameters of the beam are: ρ_i = 2689 kg/m^3, E_i = 71 GPa, m_i = 0.33, $L_1 = L_3 = L_6$ = 160 mm, b_i = 20 mm, h_i = 0.5 mm, i = 1...7. And the position of the intermediate supported beam is changed with four values while that of the bilateral support beams is unchanged. Each position is denoted as Φ_i, as shown in Table 1.

In Fig. 4, the stars represent frequencies obtained from experiments, while squares are the frequencies obtained from simulations, which have almost the same values. It can be seen that the lower the order, the better the experiments and simulations agree. The error among experimental and numerical results probably arises from the gravity effect, small difference of boundary conditions and dimensions.

The directions of the excitation and gravity are perpendicular, but the beam is still affected by gravity. The constraints of the beam with bolts in the experiment are merely an approximation of the ideal boundary condition in the theoretical model. However, it can be concluded that the above theoretical analyses are correct by simultaneously considering the results in Fig. 2 and Fig. 4.

5. Parametric influence

The frequency characteristics of a resonator and the arrangement of its electrodes are closely related to the frequencies and modal shapes of the sensitive component. The analysis of the influence law of its parameters is conducive to the optimal design and performance enhancement of a resonator.

5.1 Influence of the length of each part

Keeping the structural form of the multi-point supported beam unchanged, the lengths of the resonant beam or supported beams are changed to analyze the variation of the frequencies of the structure. The length of each part of the resonant beam is set as $L_2 = L_4 = L_5 = L_7 = L$, and the other parameters remain unchanged. Fig. 5(a) shows the relative change of the first four frequencies of the multi-point supported beam for different values of L. In the figure, f_{i0} means the ith-order frequency of the structure with L = 50 mm, and f_i is the ith-order frequency as L changes. As the value of L increases, the frequencies of the first four orders decrease, and the decline extents of each order frequency are different. To analyze the effect of the length of the supported beam on the frequencies of the structure, the length is set as $L_1 = L_3 = L_6 = \bar{L}$. and the rest of the parameters remain the same. Fig. 5(b) gives the relative change of the first four orders of frequencies of the multi-point support beam when L is taken to different values. With the increase of the length of the supported beams, the first-order frequency decreases firstly rapidly and then gently, the second-order frequency decreases approximately linearly and monotonically, the third-order frequency has a maximum value near $\bar{L}$ = 80 mm, and the fourth-order frequency remains nearly steady. The second-order frequency is almost linearly changing as the length of the

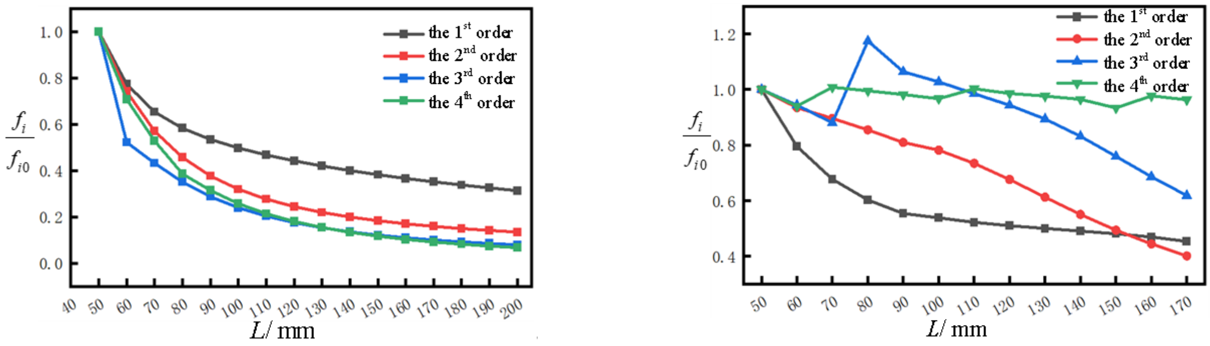

(a) Effect of the length of the resonant beam

(b) Effect of the length of the supported beams

Fig. 5 Effects of geometrical parameters on the frequencies

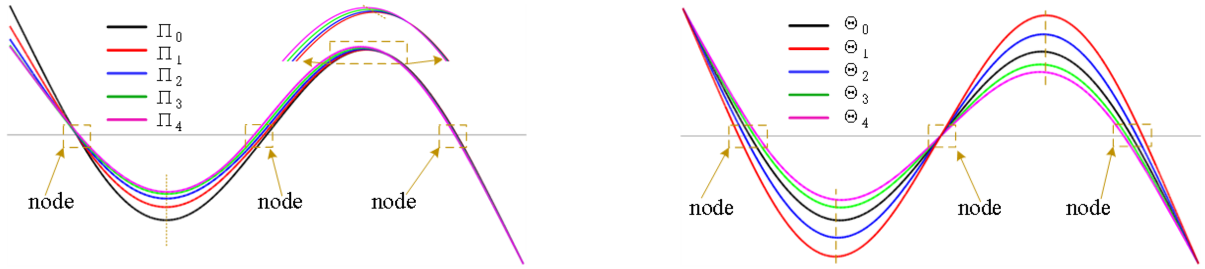

(a) The intermediate support beam (b) The bilateral support beams

Fig. 6 The influence of the position of the supported beam

supported beams increases, which is different from other frequencies. The excellent linearity makes the second-order modal shape the best choice for exciting the resonator. By comparing Fig. 5, it can be seen that the length of the resonant beam has a greater effect than the supported beams on the frequencies of the multi-point supported beam. It should be mentioned that the method that is used to calculate the frequencies in these two figures is theoretical, as given in Section 3.2. That means all the details of parametric influences can be illustrated.

5.2 Influence of the position of the supported beams

The second-order modal shape in Fig. 2 is commonly used in a resonator with three support beams. The energy dissipation caused by the support can be minimized when the support beam is connected to the node of the modal shape. Keeping the total length of the resonant beam unchanged, based on the same material parameters and considering the completely free state of the resonant beam, the second-order bending frequency is calculated to be 587.39 Hz. If the supported beams are connected at the nodes of the second-order bending modal shape of the resonant beam under this condition, we have $L_2 = L_5 = 74.68$ mm and $L_4 = L_7 = 26.82$ mm, which is denoted as Π_0. In order to study the influence of the position of the supported beams on the frequencies and modal shapes of the structure, the position of the intermediate supported beam is changed with four values while that of the bilateral supported beams is unchanged. Each position is denoted as ρ_i, as shown in Table 2. To investigate the effect of the positions of bilateral supported beams on the frequencies of the structure, Table 3 gives four sets of structures. The position of the intermediate supported beam remains unchanged and the positions of bilateral supported beams are changed with four values, which are denoted as Θ_i.

The lengths of the supported beams are set as $L_1 = L_3 = L_6 = 93$ mm, the second-order bending frequencies of the four structures in Table 2 are 607.58 Hz, 596.02 Hz, 580.94 Hz, and 565.22 Hz, respectively. The changes in the modal shapes of the resonant beam are shown in Fig. 6(a). The second-order frequency decreases with the shift of the intermediate supported beam, and the intermediate node of the modal shape is also shifted in the same direction with the supported beam. The nodes on both sides have a very small offset. The position of the point with the max displacement on the left of the modal shape is almost not shifted, but its peak value decreases. The position of the other point with the max displacement on the right of the modal shape is shifted in the same direction as the shift of the intermediate supported beam and its peak value increases. The second-order bending frequencies of the four structures in Table 3 are 583.97 Hz, 605.33 Hz, 600.85 Hz, and 578.66 Hz, respectively. Fig. 6(b) shows the changes in the second-order modal shapes of the resonant beam when the connection positions of bilateral supported beams on both sides of the sensitive component are shifted. The second-order frequency of the sensitive component increases and then decreases as bilateral supported beams are shifted to the middle. The positions of the middle node and the two extreme points remain unchanged. The positions of bilateral nodes move in the same way as bilateral supported beams are shifted to the middle, and the peak value of the extreme point decreases.

Table 2 Parameters of structure Π_i

	Π_0	Π_1	Π_2	Π_3	Π_4
L_2/ mm	74.68	69.68	64.68	59.68	54.68
L_4/ mm	26.82	26.82	26.82	26.82	26.82
L_5/ mm	74.68	79.68	84.68	89.68	94.68
L_7/ mm	26.82	26.82	26.82	26.82	26.82

Table 3 Parameters of structure Θ_i

	Θ_1	Θ_2	Θ_0	Θ_3	Θ_4
L_2/ mm	84.68	79.68	74.68	69.68	64.68
L_4/ mm	16.82	21.82	26.82	31.82	36.82
L_5/ mm	84.68	79.68	74.68	69.68	64.68
L_7/ mm	16.82	21.82	26.82	31.82	36.82

The resonator is directly affected by the frequencies of its sensitive component. The electrode arrangement in the resonator is closely related to the vibration mode of the resonant beam, and the connection position of the supported beams has an important effect on the energy dissipation and the quality factor of resonators. Therefore, the above findings can provide a certain theoretical basis for the optimization of the design of the beam-type resonator and the improvement of its performance.

6. Conclusions

The theoretical model of the sensitive component of a resonator has been established as a multi-point supported beam. Given the geometrical and material parameters, the theoretical calculation results are verified through simulations and experiments. The influence of structural parameters on the frequencies and modal shapes of the multi-point supported beam is further analyzed. The results show that the frequencies and modal shapes of the resonator beams are closely related to the structural parameters. The increase in the length of the resonant beam in the resonator leads to a decrease in frequencies, but the degree of change in each order frequency is different. The deviation in the connection positions between the supported beams and the resonant beam affects both the frequencies and the modal shapes, which leads to a change in the nodal positions of the modal shapes of the resonant beam. This insight into the relationship between the vibration characteristics and the resonators' structural parameters is valuable, as the fabrication of resonators inevitably introduces errors, which may lead to difficulties in resonator excitation and energy dispassion. Furthermore, theoretical analyses on modal shapes lay the foundation for nonlinear dynamic studies.

Acknowledgments

This work was financially supported by the National Natural Science Foundation of China (Nos. 11702188, 12002236, 12372021 and 12072233), the China Scholarship Council (202308120096), Chongqing Engineering Research Center for Advanced Intelligent Manufacturing Technology (ZNZZXDJS202003), and the Science and Technology Research project of the Chongqing Education Commission, China (KJQN202401211).

Conflict of interest

The authors declare that they have no conflicts of interest.

References

Akhavan, H., Ehyaei, J. and Ghadiri, M. (2022), "Dynamic analysis of magnetorheological elastomer sandwich MEMS sensor under magnetic field", *Smart Struct. Syst., Int. J.*, **29**(5), 705-714. https://doi.org/10.12989/sss.2022.29.5.705

Alattar, B., Ghommem, M. and Puzyrev, V. (2023), "Deep learning for nonlinear characterization of electrostatic vibrating beam MEMS", *Int. J. Bifurcat. Chaos*, **33**(15), 2330038. https://doi.org/10.1142/S0218127423300380

Cao, D.X., Leadenham, S. and Erturk, A. (2015), "Internal resonance for nonlinear vibration energy harvesting", *Eur. Phys. J. Special Topics*, **224**, 2867-2880. https://doi.org/10.1140/epjst/e2015-02594-4

Chen, S.Y., Liu, J.Z. and Guo, F.L. (2017), "Evaluation of support loss in micro-beam resonators: A revisit", *J. Sound Vib.*, **411**, 148-164. https://doi.org/10.1016/j.jsv.2017.08.048

Danzi, F., Gibert, J.M., Frulla, G. and Cestino, E. (2018), "Generalized topology for resonators having n commensurate harmonics", *J. Sound Vib.*, **419**, 585-603. https://doi.org/10.1016/j.jsv.2017.10.001

Dou, S.G. and Jensen, J.S. (2016), "Optimization of hardening/softening behavior of plane frame structures using nonlinear normal modes", *Comput. Struct.*, **164**, 63-74. https://doi.org/10.1016/j.compstruc.2015.11.001

Erturk, A., Renno, J.M. and Inman, D.J. (2009), "Modeling of piezoelectric energy harvesting from an L-shaped beam-mass structure with an application to UAVs", *J. Intell. Mater. Syst. Struct.*, **20**(5), 529-544. https://doi.org/10.1177/1045389X08098096

Feng, H., Bu, L., Li, Z., Xu, S., Hu, B., Xu, M., Jiang, S. and Wang, X. (2023), "Multimodal MEMS vibration energy harvester with cascaded flexible and silicon beams for ultralow frequency response", *Microsyst. Nanoeng.*, **9**(1), 33. https://doi.org/10.1038/s41378-023-00500-8

Georgiades, F., Warminski, J. and Cartmell, M.P. (2013), "Linear modal analysis of L-shaped beam structures", *Mech. Syst. Signal Process.*, **38**(2), 312-332. https://doi.org/10.1016/j.ymssp.2012.12.006

Habib, G., Fainshtein, E., Wolf, K.D. and Gottlieb, O. (2022), "The influence of nonlinear damping on the response of a piezoelectric cantilever sensor in a symmetric or asymmetric configuration", *Smart Struct. Syst., Int. J.*, **30**(3), 239-243. https://doi.org/10.12989/sss.2022.30.3.239

Hajjaj, A.Z., Jaber, N., Ilyas, S., Alfosail, F.K. and Younis, M.I. (2020), "Linear and nonlinear dynamics of micro and nano-resonators: Review of recent advances", *Int. J. Non-Linear Mech.*, **119**, 103328. https://doi.org/10.1016/j.ijnonlinmec.2019.103328

Hossain, N., AI Mahmud, M.Z., Hossain, A., Rahman, M.K., Islam, M.S., Tasnim, R. and Mobarak, M.H. (2024), "Advances of materials science in MEMS applications: A review", *Results Eng.*, **22**, 102115. https://doi.org/10.1016/j.rineng.2024.102115

Iliuk, I., da Fonseca Brasil, R.M.L.R., Balthazar, J.M., Tusset, A.M., Piccirillo, V. and Piqueira, J.R.C. (2014), "Potential application in energy harvesting of intermodal energy exchange in a frame: FEM analysis", *Int. J. Struct. Stabil. Dyn.*, **14**(8), 1440027. https://doi.org/10.1142/S0219455414400276

Jujjuvarapu, S.K., Devsoth, L., Akarapu, A., Pal, P. and Pandey, A.K. (2024), "Frequency and damping analysis of hexagonal microcantilever beams", *Sensors Actuators A: Phys.*, **375**, 115542. https://doi.org/10.1016/j.sna.2024.115542

Karami, M.A. and Inman, D.J. (2011), "Analytical modeling and experimental verification of the vibrations of the zigzag microstructure for energy harvesting", *J. Vib. Acoust.*, **133**(1), 011002. https://doi.org/10.1115/1.4002783

Kumar, P., Pawaskar, D.N. and Inamdar, M.M. (2024), "Investigation of a bandpass filter based on nonlinear modal coupling via 2: 1 internal resonance of electrostatically actuated clamped-guided microbeams", *J. Vib. Eng. Technol.*, **12**(3), 3783-3796. https://doi.org/10.1007/s42417-023-01084-3

Liu, Z., Chen, Y., Wang, X., Xu, Y., Dai, H., Shi, Z. and Huan, R. (2024), "Nonlinearity enhanced mode localization in two coupled MEMS resonators", *Int. J. Mech. Sci.*, **271**, 109133. https://doi.org/10.1016/j.ijmecsci.2024.109133

Ma, C., Wang, J., Shi, K., Kong, Z., Yang, W., Chen, S. and Guo, F. (2024), "Nonlinear support loss in micro/nano beam resonators induced by geometric nonlinearity", *Acta Mechanica Sinica*, **40**(3), 423180. https://doi.org/10.1007/s10409-023-23180-x

Mohammadimehr, M. and Monajemi, A.A. (2016), "Nonlinear vibration analysis of MSGT boron-nitride micro ribbon based mass sensor using DQEM", *Smart Struct. Syst., Int. J.*, **18**(5), 1029-1062. https://doi.org/10.12989/sss.2016.18.5.1029

Raman, A., Melcher, J. and Tung, R. (2008), "Cantilever dynamics in atomic force microscopy", *Nano Today*, **3**(1-2), 20-27.

https://doi.org/10.1016/S1748-0132(08)70012-4

Ranji, A.R., Guo, J., Alirezaee, S. and Ahamed, M.J. (2023), "Modelling and dynamic analysis of a MEMS ring resonator supported by circular curved shaped inner beams", *Physica Scripta*, **98**(9), 095227. https://doi.org/10.1088/1402-4896/acecbf

Romero, E., Valenzuela, V.M., Kermany, A.R., Sementilli, L., Iacopi, F. and Bowen, W.P. (2020), "Engineering the dissipation of crystalline micromechanical resonators", *Phys. Rev. Appl.*, **13**(4), 044007. https://doi.org/10.1103/PhysRevApplied.13.044007

Thrust, I. (2025), "Dynamic modeling and theoretical analysis of planar nonlinear vibrations of an articulated hoop truss antenna", *Int. J. Struct. Stabil. Dyn.*, **35**, 2550053. https://doi.org/10.1142/S0219455425500531

Tripathi, A. and Bajaj, A.K. (2013), "Computational synthesis for nonlinear dynamics based design of planar resonant structures", *J. Vib. Acoust.*, **135**(5), 051031. https://doi.org/10.1115/1.4024845

Wang, X., Xiao, D., Zhou, Z., Chen, Z., Wu, X. and Li, S. (2011), "Support loss for beam undergoing coupled vibration of bending and torsion in rocking mass resonator", *Sensors Actuators A*: *Phys.*, **171**(2), 199-206. https://doi.org/10.1016/j.sna.2011.08.023

Warminski, J., Cartmell, M.P., Bochenski, M. and Ivanov, I. (2008), "Analytical and experimental investigations of an autoparametric beam structure", *J. Sound Vib.*, **315**(3), 486-508. https://doi.org/10.1016/j.jsv.2008.01.048

Vyas, A., Peroulis, D. and Bajaj, A.K. (2009), "A microresonator design based on nonlinear 1:2 internal resonance in flexural structural modes", *J. Microelectromech. Syst.*, **18**(3), 744-762. https://doi.org/10.1109/JMEMS.2009.2017081

Zhang, W., Hu, W.H., Cao, D.X. and Yao, M.H. (2016), "Vibration frequencies and modes of a Z-shaped beam with variable folding angles", *J. Vib. Acoust.*, **138**(4), 041004. https://doi.org/10.1115/1.4033196

Zhou, S.X., Chen, W.J., Malakooti, M.H., Cao, J.Y. and Inman, D.J. (2017), "Design and modeling of a flexible longitudinal zigzag structure for enhanced vibration energy harvesting", *J. Intell. Mater. Syst. Struct.*, **28**(3), 367-380. https://doi.org/10.1177/1045389X16645

Appendix A

$$A_i = b_i h_i, \quad K_{i\eta} = \frac{E_i b_i^3 h_i}{12}, \quad K_{i\zeta} = \frac{E_i h_i^3 b_i}{12} \tag{A1}$$

$$K_{i\xi} = \frac{E_i h_i^3 b_i}{6(1+\mu)} \left\{ 1 - \frac{192 h_i}{\pi^5 b_i} \sum_{n=1}^{\infty} \frac{tanh\left[\frac{(2n-1)\pi b_i}{2h_i}\right]}{(2n-1)^5} \right\} \tag{A2}$$

$$J_{i\xi} = \frac{b_i^3 h_i + h_i^3 b_i}{12}, \quad J_{i\eta} = \frac{b_i^3 h_i}{12}, \quad J_{i\zeta} = \frac{h_i^3 b_i}{12} \tag{A3}$$

$$\begin{aligned} \kappa_{i\xi} &= \theta_i{}' + v_i{}'' w_i{}', \\ \kappa_{i\eta} &= w_i{}'' \left(\frac{\theta_i^2}{2} - \frac{w{}'^2_i}{2} - 1 \right) + \theta_i v_i{}'' \end{aligned} \tag{A4}$$

$$\kappa_{i\zeta} = v_i{}'' \left(1 - \frac{\theta_i^2}{2} + \frac{v{}'^2_i}{2} \right) + (\theta_i + v_i{}' w_i{}') w_i{}'' \tag{A5}$$

$$\begin{aligned} \omega_{i\xi} &= \dot{\theta}_i + \dot{v}_i{}' w_i{}', \\ \omega_{i\eta} &= \dot{w}_i{}' \left(\frac{\theta_i^2}{2} - \frac{w{}'^2_i}{2} - 1 \right) + \theta_i \dot{v}_i{}' \end{aligned} \tag{A6}$$

$$\omega_{i\zeta} = \dot{v}_i{}' \left(1 - \frac{\theta_i^2}{2} + \frac{v{}'^2_i}{2} \right) + (\theta_i + v_i{}' w_i{}') \dot{w}_i{}' \tag{A7}$$

where, b_i and h_i are respectively the width and thickness of the *i*th part, η is the Poisson' ratio.

Appendix B

$$u_i(0) = 0, \quad v_i(0) = 0, \quad v_i{}'(0) = 0, \quad w_i(0) = 0 \tag{B1}$$

$$\begin{aligned} &\left. \frac{\partial H_i}{\partial u_i{}'} \right|_{x_i = L_i} - \sum_{j=1}^{7} \int_0^{L_j} \frac{\partial^2 H_j}{\partial \dot{u}_i(L_i) \partial t} dx_j = 0, \\ &w_i(0) = 0 \end{aligned} \tag{B2}$$

$$\begin{aligned} &\left. \left(\frac{\partial H_i}{\partial w_i{}'} - \frac{\partial^2 H_i}{\partial w_i{}'' \partial x_i} - \frac{\partial^2 H_i}{\partial \dot{w}_i{}' \partial t} \right) \right|_{x_i = L_i} \\ &- \sum_{j=1}^{7} \int_0^{L_j} \frac{\partial^2 H_j}{\partial \dot{w}_i(L_i) \partial t} dx_j = 0 \end{aligned} \tag{B3}$$

$$\left. \left(\frac{\partial H_i}{\partial w_i{}''} \right) \right|_{x_i = L_i} - \sum_{j=1}^{7} \int_0^{L_j} \frac{\partial^2 H_j}{\partial \dot{w}_i{}'(L_i) \partial t} dx_j = 0 \tag{B4}$$

$$\begin{aligned} &\theta_i(0) = 0, \\ &\left. \frac{\partial H_i}{\partial \theta_i{}'} \right|_{x_i = L_i} - \sum_{j=1}^{7} \int_0^{L_i} \frac{\partial^2 H_j}{\partial \dot{\theta}_i(L_i) \partial t} dx_j = 0 \end{aligned} \tag{B5}$$

$$\begin{aligned} &\left. \left(\frac{\partial H_i}{\partial v_i{}'} - \frac{\partial^2 H_i}{\partial v_i{}'' \partial x_i} - \frac{\partial^2 H_i}{\partial \dot{v}_i{}' \partial t} \right) \right|_{x_i = L_i} \\ &- \sum_{j=1}^{7} \int_0^{L_j} \frac{\partial^2 H_j}{\partial \dot{v}_i(L_i) \partial t} dx_j = 0 \end{aligned} \tag{B6}$$

$$\left. \left(\frac{\partial H_i}{\partial v_i{}''} \right) \right|_{x_i = L_i} - \sum_{j=1}^{7} \int_0^{L_j} \frac{\partial^2 H_j}{\partial \dot{v}_i{}'(L_i) \partial t} dx_j = 0 \tag{B7}$$

$$\begin{aligned} (v_1' + \theta_2 + v_3')\big|_{x_i = L_i} &= 0, \\ (\theta_1 - v_2' + \theta_3)\big|_{x_i = L_i} &= 0 \end{aligned} \tag{B8}$$

$$(v_1 - \theta_1 x_2 + v_2 + (\theta_2 + v_1') x_3 + v_3)\big|_{x_i = L_i} = 0 \tag{B9}$$

$$(u_1 - w_2 + u_3 - w_1' x_2)\big|_{x_i = L_i} = 0 \tag{B10}$$

$$(w_1 + w_3 + u_2 + (w_1' + w_2') x_3)\big|_{x_i = L_i} = 0 \tag{B11}$$

$$\begin{aligned} (w_1' + w_2' + w_3')\big|_{x_i = L_i} &= 0, \\ (\theta_1 + v_5' + \theta_6)\big|_{x_i = L_i} &= 0 \end{aligned} \tag{B12}$$

$$(v_1 + \theta_1 x_5 + v_5 + (-\theta_5 + v_1') x_6 + v_6)\big|_{x_i = L_i} = 0 \tag{B13}$$

$$\begin{aligned} (v_1' - \theta_5 + v_6')\big|_{x_i = L_i} &= 0, \\ (w_1' + w_5' + w_6')\big|_{x_i = L_i} &= 0 \end{aligned} \tag{B14}$$

$$(w_1 + w_6 - u_5 + (w_1' + w_5') x_6)\big|_{x_i = L_i} = 0 \tag{B15}$$

$$(u_1 + w_5 + u_6 + w_1' x_5)\big|_{x_i = L_i} = 0 \tag{B16}$$

Appendix C

$$u_1{}^* = u_1,\ \ u_2{}^* = u_2 - w_1\big|_{x_1=L_1} \tag{C1}$$

$$u_3{}^* = u_3 - (u_1 - w_2 - x_2 w_1')\big|_{x_1=L_1,x_2=L_2} \tag{C2}$$

$$u_4{}^* = u_4 - (u_2 + w_1)\big|_{x_1=L_1,x_2=L_2} \tag{C3}$$

$$u_5{}^* = u_5 + w_2\big|_{x_1=L_1} \tag{C4}$$

$$u_6{}^* = u_6 - (u_1 + w_5 + x_5 w_1')\big|_{x_1=L_1,x_5=L_5} \tag{C5}$$

$$u_7{}^* = u_7 - (u_5 - w_1)\big|_{x_1=L_1,x_5=L_5} \tag{C6}$$

$$w_1{}^* = w_1,\quad w_2{}^* = w_2 - (x_2 w_1{}' - u_1)\big|_{x_1=L_1} \tag{C7}$$

$$w_3{}^* = w_3 - \Big(w_1 + u_2 + x_3(w_1{}' + w_2{}')\Big)\Big|_{x_1=L_1,x_2=L_2} \tag{C8}$$

$$\begin{aligned} &w_4{}^* \\ &= w_4 - \Big(w_2 - u_1 + x_2 w_1{}' \\ &\qquad + x_4(w_1{}' + w_2{}')\Big)\Big|_{x_1=L_1,x_2=L_2} \end{aligned} \tag{C9}$$

$$w_5{}^* = w_2 - (u_1 + x_5 w_1{}')\big|_{x_1=L_1} \tag{C10}$$

$$w_6{}^* = w_6 - [w_1 - u_5 + x_6(w_1{}' + w_5{}')]\big|_{x_1=L_1,x_5=L_5} \tag{C11}$$

$$\begin{aligned} &w_7{}^* \\ &= w_4 - [u_1 + w_5 + x_5 w_1{}' \\ &\qquad + x_7(w_1{}' + w_5{}')]\big|_{x_1=L_1,x_5=L_5} \end{aligned} \tag{C12}$$

$$\begin{aligned} &\theta_i{}^* = \theta_i,\quad v_1{}^* = v_1, \\ &v_2{}^* = v_2 - (v_1 - x_2\theta_1)\big|_{x_1=L_1} \end{aligned} \tag{C13}$$

$$\begin{aligned} &v_3{}^* \\ &= v_3 - [v_1 + v_2 + x_3(v_1' + \theta_2) - x_2\theta_1]\big|_{x_1=L_1,x_2=L_2} \end{aligned} \tag{C14}$$

$$\begin{aligned} &v_4{}^* \\ &= v_4 - [v_1 + v_2 + x_4(v_2' - \theta_1) - x_2\theta_1]\big|_{x_1=L_1,x_2=L_2} \end{aligned} \tag{C15}$$

$$v_5{}^* = v_5 - (v_1 + x_5\theta_1)\big|_{x_1=L_1} \tag{C16}$$

$$\begin{aligned} &v_6{}^* \\ &= v_6 - [v_1 + v_5 + x_6(v_1' - \theta_5) + x_5\theta_1]\big|_{x_1=L_1,x_5=L_5} \end{aligned} \tag{C17}$$

$$\begin{aligned} &v_7{}^* \\ &= v_7 - \big[v_1 + v_5 + x_7\big(v_5' + \theta_1\big) + x_5\theta_1\big]\big|_{x_1=L_1,x_5=L_5} \end{aligned} \tag{C18}$$

Appendix D

$$\lambda_{ij}^{u} = \omega_w\sqrt{\frac{\rho_i}{E_i}},\quad \lambda_{ij}^{\theta} = \omega_v\sqrt{\frac{\rho_i J_{i\xi}}{K_{i\xi}}} \tag{D1}$$

$$\lambda_{1i}^{v} = \sqrt{\frac{\rho_i A_i}{2K_{i\eta}}\left(\sqrt{\frac{J_{i\eta}^2\omega_v^4}{A_i^2} + 4\frac{K_{i\eta}\omega_v^2}{\rho_i A_i}} + \frac{J_{i\eta}\omega_v^2}{A_i}\right)} \tag{D2}$$

$$\lambda_{3i}^{v} = \sqrt{\frac{\rho_i A_i}{2K_{i\eta}}\left(\sqrt{\frac{J_{i\eta}^2\omega_v^4}{A_i^2} + 4\frac{K_{i\eta}\omega_v^2}{\rho_i A_i}} - \frac{J_{i\eta}\omega_v^2}{A_i}\right)} \tag{D3}$$

$$\lambda_{1i}^{w} = \sqrt{\frac{\rho_i A_i}{2K_{i\zeta}}\left(\sqrt{\frac{J_{i\zeta}^2\omega_w^4}{A_i^2} + 4\frac{K_{i\zeta}\omega_w^2}{\rho_i A_i}} + \frac{J_{i\zeta}\omega_w^2}{A_i}\right)} \tag{D4}$$

$$\lambda_{3i}^{w} = \sqrt{\frac{\rho_i A_i}{2K_{i\zeta}}\left(\sqrt{\frac{J_{i\zeta}^2\omega_w^4}{A_i^2} + 4\frac{K_{i\zeta}\omega_w^2}{\rho_i A_i}} - \frac{J_{i\zeta}\omega_w^2}{A_i}\right)} \tag{D5}$$